Materials Research Bulletin 47 (2012) 3463–3472

Contents lists available at SciVerse ScienceDirect

Materials Research Bulletin

journal homepage: www.elsevier.com/locate/matresbu

Effect of iron oxide loading on the phase transformation and physicochemical properties of nanosized mesoporous ZrO_2

S.N. Basahel [a], Tarek T. Ali [a,c], K. Narasimharao [a], A.A. Bagabas [b], M. Mokhtar [a,*]

[a] Chemistry Department, Faculty of Science, King Abdulaziz University, P.O. Box 80203, 21589 Jeddah, Saudi Arabia
[b] Petrochemicals Research Institute (PRI), King Abdulaziz City for Science and Technology (KACST), P.O. Box 6086, 11442 Riyadh, Saudi Arabia
[c] Chemistry Department, Faculty of Science, Sohag University, 82524 Sohag, Egypt

ARTICLE INFO

Article history:
Received 30 August 2011
Received in revised form 23 June 2012
Accepted 4 July 2012
Available online 24 July 2012

Keywords:
Nanostructures
Chemical synthesis
Raman spectroscopy
X-ray diffraction
Crystal structure

ABSTRACT

Mesoporous ZrO_2-supported iron oxide materials were prepared with nominal loadings of iron oxide of 5, 10, 15 and 20 wt.% using a modified co-precipitation method. The physicochemical properties of the catalysts were characterized by thermogravimetric analysis, differential scanning calorimetry, X-ray diffraction, Raman spectroscopy, high resolution transmission electron microscopy, N_2 adsorption, X-ray photoelectron spectroscopy and infrared spectroscopy methods. A delay in the ZrO_2 phase transformation as a result of the incorporation of iron was determined using TG/DSC measurements. XRD, Raman spectroscopy and HRTEM results revealed that an increase of iron oxide loading from 5 to 15 wt.% enhanced the transformation of the monoclinic to tetragonal phase. Unexpectedly, 20 wt.% iron oxide loading was required for complete tetragonal structure stabilization due to the mesoporosity of the ZrO_2 support. Iron oxide loadings from 5 to 15 wt.% showed an increase in the BET-surface area due to the presence of amorphous iron oxide on the surface. XPS and FTIR results indicated that increasing the iron oxide content to 20 wt.% resulted in stabilization of the tetragonal zirconia phase as a result of surface-to-bulk migration and incorporation of Fe^{3+} ions in the ZrO_2 lattice.

1. Introduction

One of the recent significant advances in materials science is the capability to fabricate materials with a well-defined morphology and composition on a nanometer scale. Such materials possess mechanical, electrical, optical, electrochemical, catalytic, and structural properties, which are a function of their nanostructure [1]. Zirconium dioxide (ZrO_2) is an important oxide that has been used extensively for heterogeneous catalytic reactions and in other applications because of its versatile structural and surface chemical properties as well as good thermal stability [2,3]. Furthermore, ZrO_2 has been reported to be a better catalyst and catalyst support than classical materials such as Al_2O_3, SiO_2 and TiO_2 [4]. Different ZrO_2 crystalline isomorphs can be synthesized, and the following isomorphs can be generated by controlling the preparation and pretreatment conditions: monoclinic (m-ZrO_2), tetragonal (t-ZrO_2), cubic (c-ZrO_2) and orthorhombic. Of these, t-ZrO_2 shows enhanced textural properties and lability and has oxygen atoms that can be readily exchanged; thus, this phase is suitable for numerous catalytic reactions [5]. In addition, the stabilization of t-ZrO_2 is considered the reason for the superiority of this catalyst for both activity and selectivity [6]. However, it should be noted that t-ZrO_2 is only stable at high temperatures (greater than 700 °C). Stabilization of the tetragonal phase at low temperatures is possible by introducing suitable cations, such as Ca^{2+}, Mg^{2+}, Gd^{3+}, and Y^{3+} (oversized dopants, the ionic radii are bigger than the Zr^{4+} radius) and Fe^{3+} and Ga^{2+} (undersized dopants) into the ZrO_2 structure.

Stefanic et al. [7] showed that the incorporation of Fe^{3+} into ZrO_2 has both a stabilizing and destabilizing influence on the cubic or tetragonal phase of ZrO_2. Davison et al. [8] reported the formation of solid solutions between α-Fe_2O_3 and ZrO_2 using a thermal decomposition method. After calcination in air at 600 °C, they found tetragonal solid solutions for 2.5 and 5 wt.% Fe^{3+} and cubic solid solutions for 10, 15 and 20 wt.% Fe^{3+} loadings. Using the same preparation method, the incorporation of Fe^{3+} ions within the crystal structure of t-ZrO_2 at 500 °C has been observed [9], suggesting that the pretreatment temperature is less critical than initially thought. Inwang et al. [10] reported that the formation of the ZrO_2 phase is strongly dependent on the pH of the precipitated gel. Kriventsov et al. [11] and Navio et al. [12] have prepared Fe–Zr mixed oxide gels using the co-precipitation method. They observed a mixture of m-ZrO_2 and t-ZrO_2 in the absence of iron, and it was also shown that the incorporation of iron progressively favored the formation of a tetragonal solid solution. At 5 wt.% Fe

* Corresponding author. Tel.: +966 500558045; fax: +966 26952292.
E-mail addresses: mmokhtar2000@yahoo.com, mmoustafa@kau.edu.sa (M. Mokhtar).

0025-5408/$ – see front matter © 2012 Elsevier Ltd. All rights reserved.
http://dx.doi.org/10.1016/j.materresbull.2012.07.003

loading, they observed complete formation of *t*-ZrO_2. Thus, it is clear that the preparation method has a strong influence on the degree of incorporation of iron ions, either di- or tri-valent, into the monoclinic, tetragonal and cubic ZrO_2 lattices.

Ji et al. [13] used the XAFS technique to characterize Fe-supported ZrO_2 materials and observed the formation of well-dispersed Fe^{3+} oxides at very low loading of Fe (0.5 wt.%). Boot et al. [14] supported Fe oxides on ZrO_2 and suggested the formation of α-Fe_2O_3 particles in a bimodal size distribution (7 nm and 12 nm), and they also studied the catalytic behavior of these catalysts for the dehydrogenation of butene. Okamoto et al. [6] reported that at low Fe content (less than 5 wt.%), Fe/ZrO_2 catalysts exhibited a high catalytic activity in the NO–CO reaction. The same authors [15] investigated a 5 wt.% Fe/ZrO_2 catalyst at different calcination temperatures. It was shown that when Fe/ZrO_2 was calcined below 300 °C, small particles of hydrated Fe^{3+} oxyhydroxides were formed together with Fe^{3+} cation species and ion-exchanged with the surface –OH groups of the ZrO_2. In addition to the Fe^{3+} ion-exchanged species, Fe^{3+} oxide clusters and crystalline α-Fe_2O_3 particles are formed upon calcination at 700 °C. When Fe/ZrO_2 is calcined at 800 °C and above, crystalline α-Fe_2O_3 predominates with a small amount of the Fe^{3+} cations present in the vacant sites. It has been found that the Fe^{3+} oxide clusters are catalytically active for NO–CO reactions, while ion-exchanged Fe^{3+} species and crystalline α-Fe_2O_3 are considerably less active. The catalytic activity of Fe/ZrO_2 decreases as the calcination temperature increases and becomes completely inactive when calcined at 800 °C. The authors concluded that the catalytically active Fe^{3+} oxide clusters are gradually consumed by a reaction with ZrO_2 to form the Fe^{3+} species in the surface vacant sites and by sintering to form α-Fe_2O_3 at high calcination temperatures. With low Fe loadings, the dissolution of Fe ions in the ZrO_2 lattice was observed, and it was noted that this process makes the resultant solid solution a less catalytically active material. Stefanic et al. [7] determined the solubility limits of Fe_2O_3 in the lattice of ZrO_2 and observed that the terminal solubility limit of Fe_2O_3 in ZrO_2 is approximately 33 mol%.

Despite a number of studies on the influence of Fe_2O_3 on the stabilization of the ZrO_2 structure and its subsequent effect on catalytic performance in various reactions, an understanding of the differing interactions between Fe_2O_3 and the surface of ZrO_2 at low calcination temperatures and high Fe loadings is considerably limited. The aim of our study was to explore the possibility of generating catalytically active Fe^{3+} clusters on the surface of mesoporous ZrO_2 by incorporating high amounts of iron. In this report, we used a modified co-precipitation method to prepare highly dispersed nanoscale mesoporous iron-loaded ZrO_2 catalysts. The effect of iron oxide loading on the phase transformation of ZrO_2 at relatively low calcination temperatures was studied.

2. Experimental

2.1. Materials

All reagents were analytical grade and used as received without purification. Zirconyl chloride octahydrate ($ZrOCl_2{\cdot}8H_2O$), ferric nitrate nonahydrate ($FeNO_3)_3{\cdot}9H_2O$, and ammonium hydroxide solution were purchased from Aldrich, U.K.

2.2. Synthesis of iron oxide-supported ZrO_2 nanomaterials

Iron oxide/ZrO_2 solid specimens were prepared using a modified co-precipitation method with two solutions, (A) and (B). Solution (A) contained 0.8 mol/L of $ZrOCl_2{\cdot}8H_2O$, and solution (B) consisted of different amounts of $Fe(NO_3)_3{\cdot}9H_2O$ that corresponded to 0.0, 5.0, 10.0, 15.0 and 20.0 wt.%. Aqueous ammonium hydroxide (Aldrich, 20 wt.%) was added dropwise to the mixtures of solutions A and B with continuous stirring at pH 9. The pH of the total solution was maintained at *ca.* 9 under vigorous stirring at 30 °C for 2 h. The precipitate was then aged at 85 °C for 48 h in a water bath. The aged precipitate was filtered and washed several times until the precipitate was free from excess chloride ions. The precipitate was subsequently dried at 90 °C for 3 h. Portions of the synthesized materials were calcined at 500 °C with a ramp rate of 1 °C min^{-1} and kept at this temperature for 3 h. The calcined materials were annotated using the following: *x*-FeZr-500, where *x* = 0, 5, 10, 15 and 20 wt.%.

2.3. Characterization

Thermal gravimetric analysis (TGA) and differential scanning calorimetry (DSC) were carried out using a computerized Shimadzu Thermal Analyzer TA60 Apparatus (Japan). A ceramic sample boat was used for the TGA analysis. Samples weighing 10 ± 0.1 mg were heated to 1000 °C at 10 °C min^{-1} in a flow of 40 mL min^{-1} N_2 gas. For the DSC measurements, aluminum open pans (without lids) were used to allow interaction of the sample with the DSC cell atmosphere. Samples weighing 5 ± 0.1 mg were heated to 500 °C at 10 °C $min^{-1}$with a flow rate of 40 mL min^{-1}.

X-ray powder diffraction (XRD) studies were performed for all of the prepared solid samples using a Bruker diffractometer (Bruker D8 advance target). The patterns were run with copper $K_{\alpha 1}$ and a monochromator (λ = 1.5405 Å) at 40 kV and 40 mA. The crystallite size of the zirconia phase was calculated using Scherrer's equation:

$$D = \frac{B\lambda}{\beta_{1/2} \cos \theta} \quad (1)$$

where D is the average crystallite size of the phase under investigation, B is the Scherer constant (0.89), λ is wavelength of the X-ray beam used (1.54056 Å), $\beta_{1/2}$ is the full width at half maximum (FWHM) of the diffraction peak and θ is the diffraction angle. The identification of different crystalline phases in the samples was performed by comparing the data with the Joint Committee for Powder Diffraction Standards (JCPDS) files.

The Raman spectra of samples were measured with a Bruker Equinox 55 FT-IR spectrometer equipped with an FRA106/S FT-Raman module and a liquid N_2 cooled Ge detector using the 1064 nm line of a Nd:YAG laser with an output laser power of 200 mW.

A Philips CM200FEG microscope, 200 kV, equipped with a field emission gun was used for HRTEM analysis. The coefficient of spherical aberration was C_s = 1.35 mm. The information limit was better than 0.18 nm. High-resolution images with a pixel size of 0.044 nm were taken with a CCD camera.

The textural properties of the prepared samples were determined from nitrogen adsorption/desorption isotherm measurements at −196 °C using a model NOVA 3200e automated gas sorption system (Quantachrome, U.S.A.). Prior to measurement, each sample was degassed for 6 h at 150 °C. The specific surface area, S_{BET}, was calculated by applying the Brunauer–Emmett–Teller (BET) equation. The average pore radius was estimated from the relation $2V_p/S_{BET}$, where V_p is the total pore volume (at P/P_0 = 0.975). Pore size distribution over the mesopore range was generated by the Barrett–Joyner–Halenda (BJH) analysis of the desorption branches, and the values for the average pore size were calculated.

The XPS measurements were carried out by using a SPECS GmbH X-ray photoelectron spectrometer. Prior to analysis, the samples were degassed under vacuum inside the load lock for 16 h. The binding energy of the adventitious carbon (C 1s) line at

284.6 eV was used for calibration, and the positions of other peaks were corrected according to the position of the C 1s signal. For the measurements of high resolution spectra, the analyzer was set to the large area lens mode with energy steps of 25 meV and in Fixed Analyzer Transmission (FAT) mode with pass energies of 34 eV and dwell times of 100 ms. The photoelectron spectra of the four samples were recorded with the acceptance area and angle of 5 mm in diameter and up to ±5°, respectively. The base pressure during all measurements was 5×10^{-9} mbar. A standard dual anode excitation source with Mg Kα (1253.6 eV) radiation was used at 13 kV and 100 W.

FTIR spectra were recorded on a Perkin-Elmer Spectrum 100 FTIR spectrometer using KBr pellets (1 wt.% sample in KBr matrix).

3. Results and discussion

3.1. Thermogravimetric (TGA) and differential scanning calorimetric (DSC) analyses

The TGA patterns of the prepared samples are presented in Fig. 1. The pure ZrO_2 sample showed a two stage weight loss process: the first at 50 °C and the second at approximately 140 °C. The initial weight loss of 9% was attributed to the desorption of physically adsorbed water. The second weight loss of 20% was thought to be due to the thermal evolution of chemically bonded water molecules from the surface of ZrO_2. Similar results have been observed by Matos et al. [16] with nanocrystalline ZrO_2. The decomposition process of 5-FeZr, 10-FeZr and 15-FeZr samples is similar to pure ZrO_2, except that incorporation of Fe causes a shift in the decomposition temperature of the chemically bonded water molecules. The second weight loss occurred at 170 °C for the 5-FeZr and 10-FeZr samples, whereas this process took place at 200 °C for the 15-FeZr sample. The reason for this temperature shift could be due to presence of hydrated amorphous iron hydroxides. The 20-FeZr sample showed a three-step decomposition process. The first occurred from room temperature to 80 °C, corresponding to a weight loss of 10.6% and was attributed to the loss of physisorbed water. The second occurred at approximately 240 °C, with a weight loss of 23%, while the third weight loss occurred at approximately 405 °C with a 59% weight loss. The second weight loss was due to further dehydration, followed by the hydrous ZrO_2 being progressively decomposed into amorphous ZrO_2 due to dehydroxylation as the temperature increases.

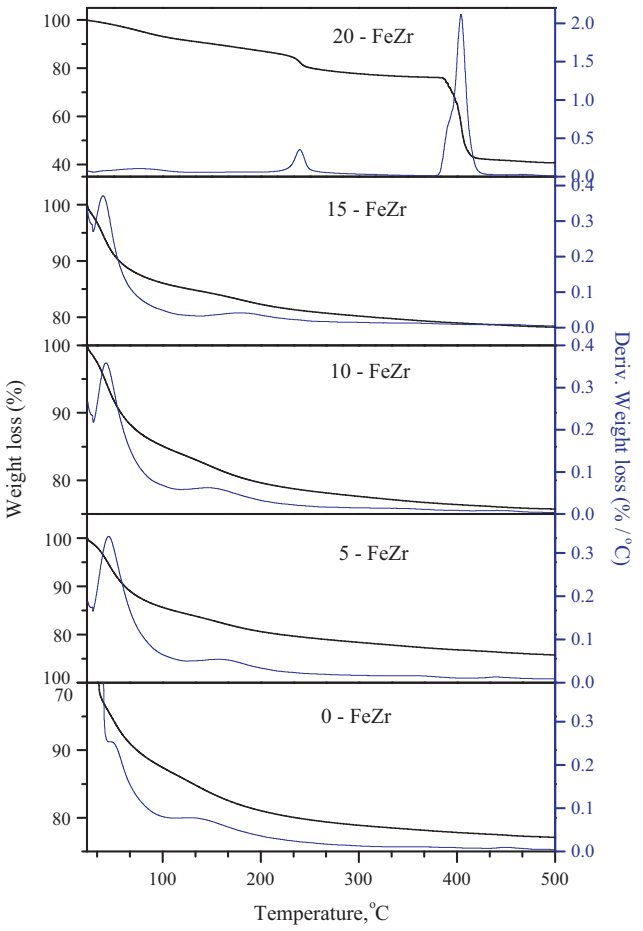

Fig. 1. TGA and DTG thermograms of prepared ZrO_2 and iron oxide-supported ZrO_2 samples.

The DSC patterns of all of the sample precursors are shown in Fig. 2. Two endothermic peaks at 65 °C and 150 °C and two exothermic peaks at 245 °C and 470 °C were observed with pure ZrO_2. The DSC patterns of Fe-loaded samples showed a similar pattern to pure ZrO_2. The appearance of these endothermic and exothermic peaks agrees with the TGA results reported by other researchers [17]. The two exothermic DSC peaks were present in all of the Fe-incorporated samples, but the temperature maximum was shifted to higher temperatures for the 15-FeZr and 20-FeZr samples. The delay in the crystallization of ZrO_2 was more pronounced when iron hydroxide was co-precipitated with zirconium hydroxide. The first exothermic peak observed at 245 °C could be due to the decomposition of NH_3 species attached to Zr or Fe oxides. The intensity of this peak increased with an increase in iron content. The high temperature exothermic peak at approximately 470 °C is associated with the nucleation of the amorphous material to form the ZrO_2 polymorph. Aguilar et al. [18] reported that the first structure to crystallize is the tetragonal form, which occurs between 300 and 500 °C, followed by its transformation to the monoclinic form, which occurs between 900 and 1000 °C. Moreover, the greater the iron content was in the sample, the longer the delay in the crystallization temperature was.

3.2. Powder X-ray diffraction

Powder X-ray diffraction patterns of pure ZrO_2 and the supported Fe/ZrO_2 samples calcined at 500 °C are presented in Fig. 3. The 0-FeZr-500 sample showed a mixture of monoclinic and tetragonal ZrO_2 crystalline phases. The lines at 28.5°, 31.5°and 34.4° were attributed to ZrO_2 in the monoclinic form (JCPDS No. 78 0047). The lines at $2\theta = 30.4°$ and 35.3° indicated the presence of ZrO_2 in the tetragonal (JCPDS No. 80 2156) or cubic phase. The tetragonal structure can be distinguished from the cubic structure by the presence of characteristic splitting of the diffraction peaks [19]. Splitting of the diffraction peaks was not observed in the XRD patterns of the iron-supported samples, indicating the absence of the cubic structure of ZrO_2 in these samples. Further analysis was conducted by Raman spectroscopy to confirm the crystalline phases for all of the supported samples. The volume percent of monoclinic and tetragonal phases present in the ZrO_2 was determined from the integrated intensities of the diffraction peaks $(\bar{1}\,1\,1)$, $(1\,1\,1)$ of m-ZrO_2 at $2\theta = 28.5°$ and 31.5°, respectively, and the diffraction line $(1\,0\,1)$ of t-ZrO_2 at $2\theta = 30.4°$. We used the following expressions reported in the literature [20].

$$\%M_{\text{monoclinic}} = \frac{\sum M_{\text{monoclinic}} \times 100}{T_{\text{tetragonal}} + \sum M_{\text{monoclinic}}} \quad (2)$$

$$\%T_{\text{tetragonal}} = 100 - M_{\text{monoclinic}} \quad (3)$$

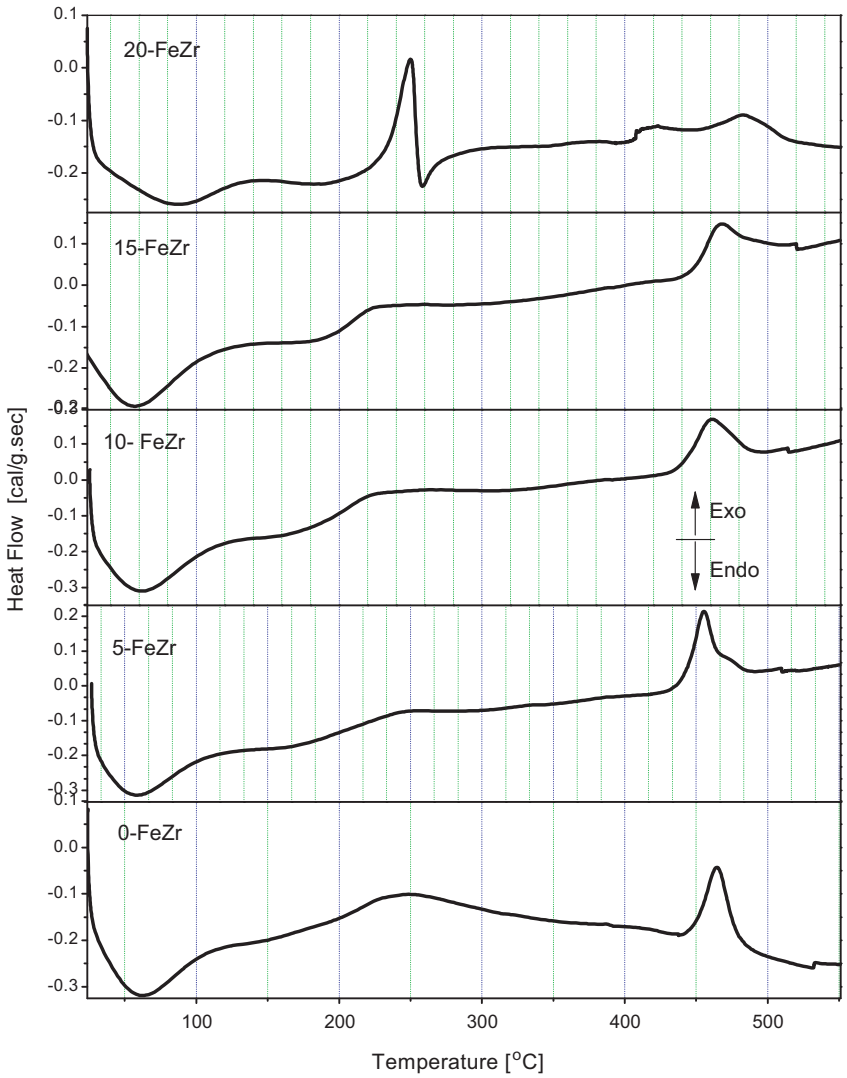

Fig. 2. DSC thermograms of prepared ZrO_2 and iron oxide-supported ZrO_2 samples.

The percentages of tetragonal and monoclinic phases and the crystallite sizes of the composites are tabulated in Table 1. Doping of Fe into the structure of ZrO_2 caused a phase transformation of ZrO_2 from the monoclinic to tetragonal phase. With an increase of iron loading from 5 to 15 wt.%, the transformation of the monoclinic to the tetragonal phase was increased. The addition of 20 wt.% iron resulted in complete transformation of ZrO_2 into the tetragonal phase. The X-ray diffraction patterns of all of the iron-loaded samples after calcination at 500 °C did not show any diffraction peaks corresponding to long-range ordered iron oxide. The absence of the prominent reflections of iron oxides indicated that no crystalline bulk materials were formed outside the pore system of the support. It is possible that nanoparticles of iron oxide might disperse uniformly in the framework of ZrO_2 or alternatively, the iron oxide species is present as relatively small particles (below the powder X-ray detection limit). Davison et al. [8] prepared Fe/ZrO_2 samples by thermal decomposition of Fe and Zr precursors at 600 °C and observed the presence of a diffraction peak of α-Fe_2O_3 in the sample containing a nominal Fe composition of 30 wt.%. Okamoto et al. [15] prepared Fe/ZrO_2 catalysts using an impregnation method and reported the presence of a peak due to α-Fe_2O_3 as the Fe content increased above 2 wt.%. These results indicate that the formation of crystalline α-Fe_2O_3 particles in the pore structure of the support is highly dependent on the preparation conditions.

The average crystallite sizes (calculated using Scherrer's equation (1)) of the monoclinic and tetragonal phases were 16 and 28 nm, respectively. It has been reported that there is a critical crystallite size (approximately 30 nm) below which the tetragonal phase of ZrO_2 is stable [21]. The presence of *t*-ZrO_2 in all of the samples indicates that the crystallite size of pure ZrO_2 synthesized by our method is less than the critical size. The *t*-ZrO_2 can also be stabilized by the presence of foreign cations in the ZrO_2 lattice [22]. These ions help to restrict the motion of defects in the lattice, thereby stabilizing the tetragonal phase. In the present study, it is likely that iron oxide is anchored to the defect centers. This result, where there is a restriction in the motion of defect centers, facilitates stabilization of the tetragonal phase [23].

3.3. Raman spectroscopy

Raman spectroscopy is a very useful tool to differentiate the ZrO_2 phases present in the samples. Fig. 4 shows the Raman spectra of the Fe-supported catalysts. It has been reported that *t*-ZrO_2 exhibits typical Raman bands at 148, 263, 325, 472, 608, and 640 cm^{-1}, with a strong band at 263 cm^{-1} [24]. *m*-ZrO_2 exhibits

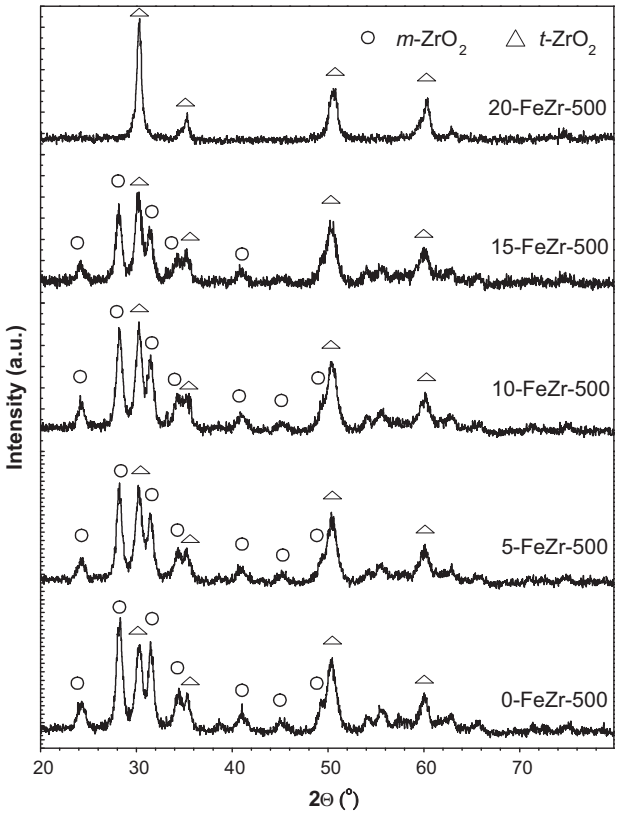

Fig. 3. Powder XRD patterns of ZrO_2 and iron oxide-supported ZrO_2 samples calcined at 500 °C.

bands at 140, 173, 185, 216, 260, 301, 328, 342, 471, 500, 553 and 632 cm^{-1}, with strong bands at 173, 185 and 472 cm^{-1} [25]. In the present study, the major phase for 5-FeZr-500 was monoclinic, with less intense peaks due to the tetragonal phase also being seen in the spectrum. The band at 263 cm^{-1}, typical of the tetragonal phase, clearly appeared in the 10, 15 and 20 wt.% samples, along with other bands indicating the monoclinic phase. The disappearance of the peaks correlating to the monoclinic phase was observed with the 20-FeZr-500 sample. The single Raman band characteristic of the cubic structure located at approximately 460 cm^{-1} was not observed in any of the samples. These results corroborate the XRD results. As opposed to the XRD analyses, Raman spectroscopy allows the determination of the α-Fe_2O_3 formation in supported samples with low iron content [26]. Raman peaks corresponding to α-Fe_2O_3 appear at 225, 245, 292, 411, 498, 611, and 1323 cm^{-1}, and Fe_3O_4 exhibits a sharp band at 663 cm^{-1} [27]. Some of the peaks resulting from the monoclinic ZrO_2 phase overlap with the bands corresponding to α-Fe_2O_3. However, the prepared iron-supported ZrO_2 samples did not show the major bands of α-Fe_2O_3 (1323 cm^{-1}) and Fe_3O_4 (663 cm^{-1}), which do not overlap with the

Table 1
Percentage of crystalline phases measured from XRD patterns and average particle size from TEM images.

Sample ID	XRD analysis		Av. particle size[a] (nm)
	Tetragonal phase (%)	Monoclinic phase (%)	
0-FeZr-500	35	65	14
5-FeZr-500	38	62	20
10-FeZr-500	48	52	24
15-FeZr-500	60	40	30
20-FeZr-500	100	0	40

[a] Measured from TEM analysis.

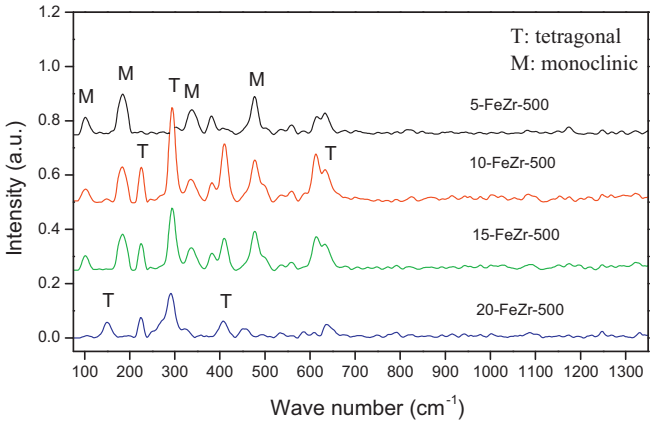

Fig. 4. Raman spectra of iron oxide-supported ZrO_2 samples calcined at 500 °C.

monoclinic phase of ZrO_2. The Raman spectroscopy results provided further evidence that there was no formation of crystalline iron oxides.

3.4. High resolution transmission electron microscopy (HRTEM)

Fig. 5(A)–(C) shows TEM images of 0-FeZr-500, 10-FeZr-500 and 20-FeZr-500, respectively. The shape of the ZrO_2 particles was spherical to semi-hexagonal. ZrO_2 is very crystalline, as demonstrated by the long-range ordering of the lattices (the image clearly shows fringes indicating the atomic layers). The particle size varied upon altering the amount of iron oxide, as tabulated in Table 1. The mean particle diameter of the ZrO_2 particles of the 5-FeZr-500 sample was 14 nm and was changed to 40 nm when the Fe loading was increased to 20 wt.%. Reproduced HRTEM images of the 0-FeZr-500, 10-FeZr-500 and 20-FeZr-500 samples are also shown in Fig. 5(D)–(F). The lattice fringes of the ZrO_2 are clearly visible in these images. Both 0-FeZr-500 and 10-FeZr-500 samples exhibited composite particles consisting of monoclinic and tetragonal parts, where the volume percentage of monoclinic was higher in the case of 0-FeZr-500 compared to the 10-FeZr-500 sample. The lattice spacing of the crystalline *t*-ZrO_2 with inter-phase spacing of $d(1\,0\,1) = 0.30$ nm was clearly observed in the HRTEM images. HRTEM showed clear lattice fringes, and the distance between two adjacent planes was measured to be 0.30 nm and 0.34 nm, corresponding to (1 0 1) planes in *t*-ZrO_2 and (1 1 1) planes in *m*-ZrO_2 [28].

In the HRTEM image of the 20-FeZr-500 sample (Fig. 5(F)), the strongest reflections belong to the *t*-ZrO_2 grain, and weak reflections belong to the iron oxide layer in the (0 1 1) orientation. The region marked is composed of *t*-ZrO_2 grain overlapping with a thin layer of iron oxide, which could serve as evidence that interaction takes place within the layers. The surface of the ZrO_2 crystallites exhibited a very thin amorphous layer of iron oxide, and the absence of crystalline iron oxide was in agreement with the XRD results.

3.5. Nitrogen physisorption

The nitrogen physisorption isotherms of ZrO_2 and Fe-supported ZrO_2 materials are shown in Fig. 6. The isotherms of the 0-FeZr-500, 5-FeZr-500 and 10-FeZr-500 samples were of type IV, with a hysteresis in the 0.7–0.9 P/P_0 region, typical of mesoporous materials. The isotherm of the 20-FeZr-500 sample showed a different pattern of the desorption path in the 0.48 P/P_0 region. The appearance of a well-defined hysteresis loop associated with irreversible capillary condensation in the mesopores of the P/P_0 region from 0.4 to 1.0 suggests the presence

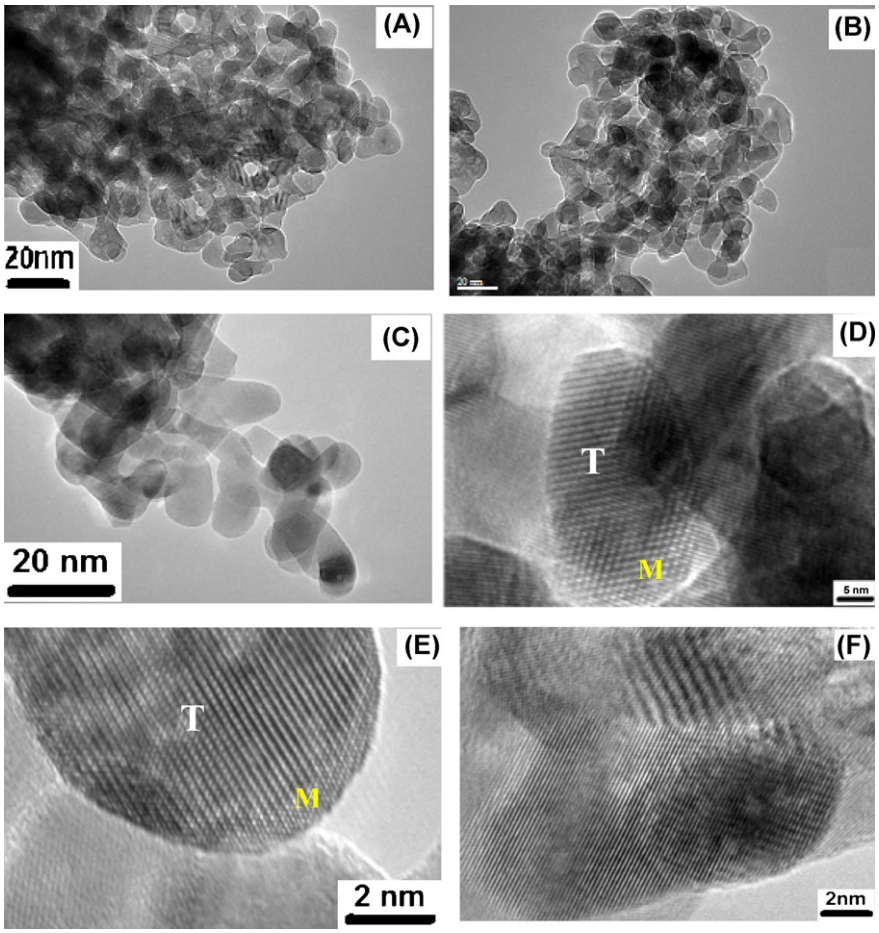

Fig. 5. TEM micrographs of (A) 0-FeZr-500, (B) 10-FeZr-500, and (C) 20-FeZr-500: HRTEM micrograph of (D) 0-FeZr-500, (E) 10-FeZr-500, and (F) 20-FeZr-500. T, tetragonal; M, monoclinic.

of mesoporosity arising from non-crystalline voids and spaces formed by interparticle contacts in the samples. The calculated textural parameters from the physisorption analysis are listed in Table 2. The capillary condensation step was more pronounced and shifted to a higher P/P_0 for the 0-FeZr-500, 5-FeZr-500 and 15-FeZr-500 samples, which is a clear indication that these materials possess a large BET surface area, pore volume and average pore diameter (Table 2). An increase of the textural properties with an increase of Fe loading from 5 to 15 wt.% was observed; this could be due to the formation of amorphous Fe oxide or mixed Fe–Zr oxides on the surface of the support. However, a loading of 20 wt.% Fe caused a significant decrease in the specific surface area, pore volume, and pore diameter; this could be due to iron oxide particle deposition within the pores of the ZrO_2 support. Partial pore blocking could also be assumed because of the changes in the desorption branch of the isotherm in the case of this sample (Fig. 6).

Fig. 7 shows the pore-size distribution plots obtained using the BJH equation from the desorption branch of the isotherm. The pore-size distribution (PSD) measurements showed that the 0-FeZr-500 sample had a broad PSD peak in the range of 100–110 Å pore radii. Incorporation of 5 wt.% Fe caused a broadening of the PSD peak. A similar broadness of the PSD peak was observed in both the 10-FeZr-500 and 15-FeZr-500 samples. It is interesting to note that the development of micropores with a pore radius of 18 Å along with mesopores was observed in the 15-FeZr-500 sample. The presence of higher amounts of amorphous Fe or Fe–Zr oxide may have contributed to the observed micropores in this sample. Contrary to the other supported samples, the 20-FeZr-500 sample did not show any mesopores and displayed a narrow PSD peak with a pore radius of 20.3 Å.

Kriventsov et al. [11] prepared a Fe/ZrO_2 catalyst using the sol–gel method by varying the Fe amounts from 1 to 20 wt.%. The surface area of the pure support was 31 $m^2\ g^{-1}$, and an increase in surface area was observed with an increase in Fe loading. The 20 wt.% Fe-loaded catalyst showed a maximum surface area of 59 $m^2\ g^{-1}$. These authors observed a complete transformation of the monoclinic to tetragonal phase after 5 wt.% of Fe loading. In the present case, we obtained mesoporous ZrO_2 with a uniform pore size and high surface area (65 $m^2\ g^{-1}$). Mesoporous ZrO_2 requires a high amount of Fe to ensure monolayer coverage, which is a possible reason for the complete monoclinic to tetragonal transformation between 15 and 20 wt.% of Fe loading.

Based on the XRD, Raman, HRTEM and N_2 adsorption measurements, it is clear that iron oxide presented as an amorphous species and was responsible for the *t*-ZrO_2 phase stabilization. However, further analysis was required to understand the nature of the interaction between the iron oxide and the support and its effect on the dispersion of iron oxide species. Therefore, XPS analysis was used to study the nature of the iron species.

3.6. XPS spectroscopy

Fig. 8(A) shows the O (1s) photoelectron transition diagram for the Fe/ZrO_2 samples. All of the pretreated Fe-supported samples showed a single O (1s) peak. The binding energy of this peak for the 5-FeZr-500, 10-FeZr-500 and 15-FeZr-500 samples was 530 eV, but

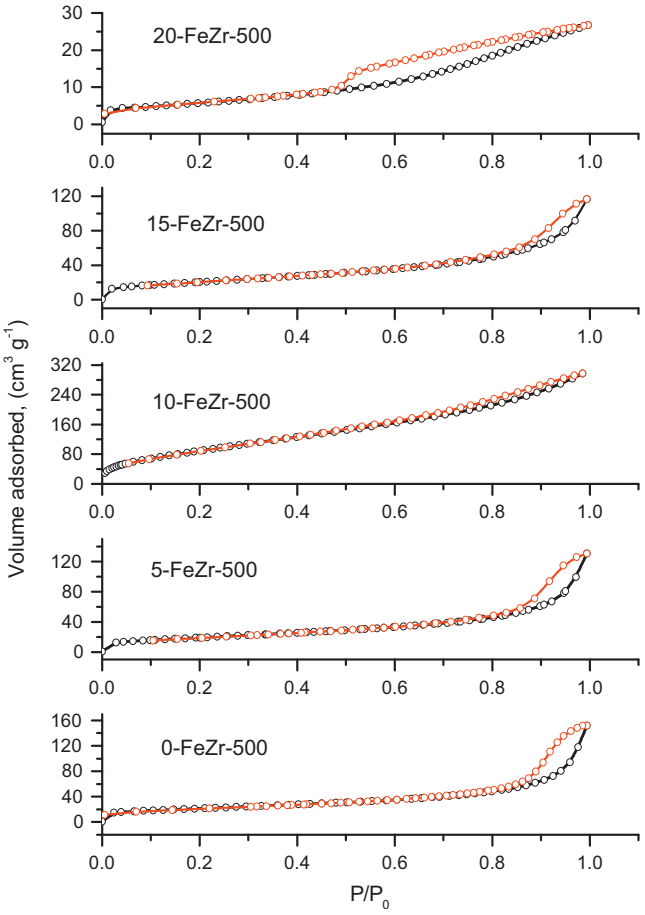

Fig. 6. Adsorption/desorption isotherms of ZrO_2 and iron oxide-supported ZrO_2 samples calcined at 500 °C.

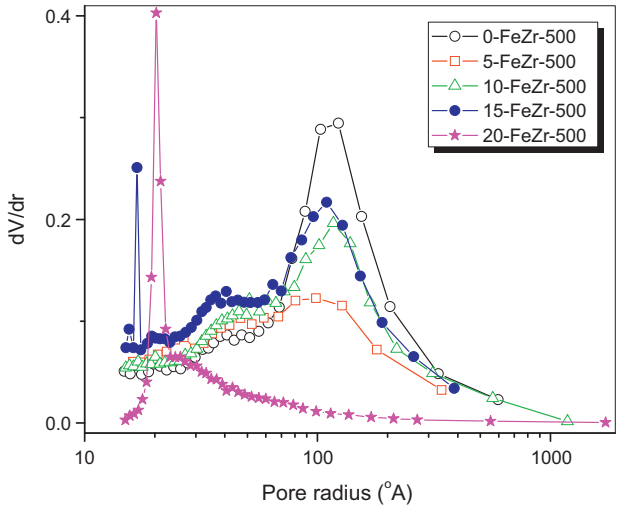

Fig. 7. Pore size distribution of ZrO_2 and iron oxide-supported ZrO_2 samples calcined at 500 °C.

was shifted to 529.0 eV for the 20-FeZr-500 sample. Navio et al. [12] assigned a binding energy of 530.0 eV to the Zr–O–Zr bonding for iron-supported catalysts. The lower value for O (1s) of 529.0 eV for the 20-FeZr-500 sample may be due to the presence of an amorphous iron oxide phase on the external surface of the ZrO_2 support. Wagner et al. [29] observed a lower binding energy value of 0.8 eV for O (1s) from Fe_2O_3 in comparison with O (1s) from ZrO_2.

The Zr ($3d_{5/2}$) components for all of the iron-supported samples are shown in Fig. 8(B). The 5-FeZr-500, 10-FeZr-500 and 15-FeZr-500 samples showed a peak at 182.4 eV, which was shifted from 182.4 to 181.9 eV for the 20-FeZr-500 sample. The shift in the XPS binding energy of Zr ($3d_{5/2}$) seems to suggest that over part of the surface, Zr^{4+} cations were reduced to a lower valence state. A similar observation was reported by Borer et al. [30], where Ru metal promoted a reduction of the Zr oxidation state for a Ru/ZrO_2 catalyst pretreated at 500 °C. This observation indicates that the presence of a high amount of iron species promotes a reduction of the Zr oxidation state.

The overlaid spectra of Fe ($2p_{3/2}$) components are shown in Fig. 8(C). Some differences were observed in the Fe $2p_{3/2}$ binding energy values for the supported samples; these were most pronounced in the 20-FeZr-500 sample. Brundle et al. [31] have shown that in bulk iron oxides, Fe(III) has a $2p_{3/2}$ binding energy of approximately 711 eV, whereas the $2p_{3/2}$ binding energy of Fe(II) is centered at approximately 709.7 eV. The differentiation between Fe(III) and Fe(II) species can be achieved by taking into consideration the satellite peak energies at 719.8 eV or 715 eV for Fe (III) or Fe (II), respectively. A satellite peak at approximately 719 eV was observed in the case of the 20-FeZr-500 sample, indicating the presence of Fe(III) due to Fe_2O_3 on the surface.

The deconvoluted spectra of the Fe ($2p_{3/2}$) components for the 5-FeZr-500, 10-FeZr-500, 15-FeZr-500 and 20-FeZr-500 samples are shown in the Fig. 8(D)–(G), respectively. The binding energies were located at 714.8, 711.0 and 704.6 eV for 5-FeZr-500. The binding energies shifted slightly with a change in Fe composition, which implies that the Fe oxidation state of surface iron species is sensitive to the Fe composition. Wandelt et al. [32] reported that the characteristic Fe ($2p_{3/2}$) peaks are located at 707, 710 and 711 eV for Fe^0, Fe^{2+} and Fe^{3+}, respectively. Grosvenor et al. [33] stated that the peak located at 715 eV can be attributed to a surface Fe peak. Droubay and Chambers [34] claimed that the surface peak is mostly caused by the Fe^{3+} cations at the surface of α-Fe_2O_3, which affects the binding energy of samples. However, it is believed that the Fe cations that are interacting with surface hydroxyls of ZrO_2 might be at a different oxidation state than the pure calcined iron oxide.

Fe ($2p_{3/2}$) binding energy values corresponding to iron oxidation states and its surface atomic composition are presented in Table 3. The atomic concentration of the Fe surface-bound peak for the 5-FeZr-500 sample was 6.3% and increased to 15.7% after the loading was increased to 10 wt.%. A further increase of Fe loading to 15 and 20 wt.% caused a decrease in the concentration of this peak to 13% and 3.8%, respectively. It is known that the Fe species formed on the surface of the ZrO_2 greatly depends on the iron oxide loading [35]. With increase of Fe loading from 5 to 10 wt.%, the contribution of the surface peak (Table 3) was increased and further increase of iron oxide loading to 15 wt.%, contribution of the peak started decreasing, and it was decreased further, when iron oxide loading increased to 20 wt.%. This phenomenon might be due to formation of less number of surface iron species in case of 5-FeZr-500 sample and concentration of surface species started increasing with increase of loading to 10 wt.%. The monolayer coverage of the mesoporous ZrO_2 support reached in between 10 wt.% and 15 wt.% loading. Further increase

Table 2
Textural properties data from N_2 physisorption isotherms.

Sample ID	S_{BET} ($m^2 g^{-1}$)	V_p ($cm^3 g^{-1}$)	Av. pore radius (Å)
0-FeZr-500	65.05	0.1830	16.4
5-FeZr-500	61.04	0.1292	16.1
10-FeZr-500	68.67	0.1603	15.6
15-FeZr-500	78.96	0.1771	16.8
20-FeZr-500	20.71	0.0412	20.3

S_{BET}, specific BET surface area; V_p, pore volume.

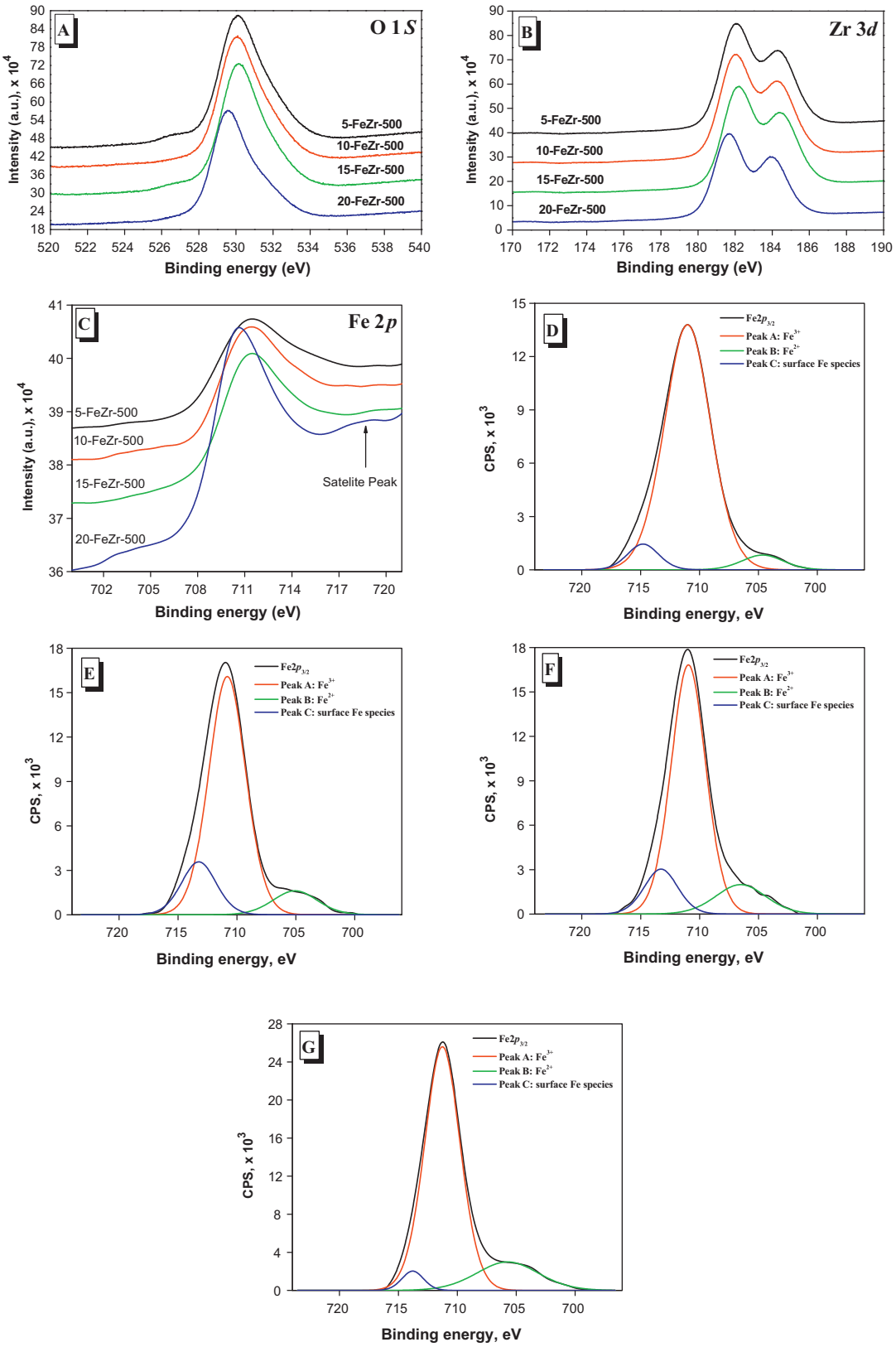

Fig. 8. (A) Overlaid XPS spectra of O (1s) components, (B) overlaid spectra of XPS Zr ($3d_{5/2}$) components, (C) overlaid XPS spectra of Fe ($2p_{3/2}$) components, (D) deconvoluted XPS Fe ($2p_{3/2}$) components for 5-FeZr-500, (E) deconvoluted XPS Fe ($2p_{3/2}$) components for 10-FeZr-500, (F) deconvoluted XPS Fe ($2p_{3/2}$) components for 15-FeZr-500 and (G) deconvoluted XPS Fe ($2p_{3/2}$) components for 20-FeZr-500.

of loading (15 and 20 wt.%, beyond monolayer) caused formation of multilayers of iron oxide bulk species, which can easily hinder the exposure of surface bound species. Because of the formation of more iron oxide multilayers on the surface of 20-FeZr-500, the contribution of the surface peak is lower than 5 wt.% loaded sample. Weckhuysen et al. [35] observed that the Fe ions preferentially reacted with the hydroxyl groups at the outer surface of the zeolite during impregnation of the precursor.

Table 3
Fe ($2p_{3/2}$) binding energy values and atomic concentration of different Fe species.

Sample ID	XPS Fe ($2p_{3/2}$) binding energy (eV)	Surface atomic conc. (%)	Phase assigned in the literature [32,33]
5-FeZr-500	714.80	6.30	Fe-surface bonded
	711.02	88.80	Fe^{3+}(Fe_2O_3, Fe_3O_4 and FeOOH)
	704.65	4.70	Fe^{2+}
10-FeZr-500	713.24	15.70	Fe-surfaced bonded
	710.82	75.10	Fe^{3+}(Fe_2O_3, Fe_3O_4 and FeOOH)
	705.06	9.00	Fe^{2+}
15-FeZr-500	713.28	13.00	Fe-surface bonded
	710.95	74.20	Fe^{3+}(Fe_2O_3, Fe_3O_4 and FeOOH)
	706.52	12.70	Fe^{2+}
20-FeZr-500	713.79	3.80	Fe-surface bonded
	711.27	79.80	Fe^{3+}(Fe_2O_3, Fe_3O_4 and FeOOH)
	705.73	16.30	Fe^{2+}

Loading of Fe beyond the monolayer coverage (20 wt.%) caused the migration of Fe cations into the crystal lattice of ZrO_2, resulting in a decrease of surface-bound Fe species. This observation was further verified by FTIR analysis.

3.7. FTIR spectroscopy

The FTIR spectra of the samples are shown in Fig. 9. The FTIR spectra of all of the calcined samples show a broadband corresponding to HO at $\nu = 3430\ cm^{-1}$ and a sharp band of adsorbed molecular water δ_{OH} at $1630\ cm^{-1}$. These bands were more intense in the samples with low iron loading, but less intense in the 20 wt.% sample. The strong IR absorption at approximately $3400\ cm^{-1}$, corresponding to the stretching vibrations of hydroxyl bonds, makes FTIR spectroscopy a very important tool for the detection of reactive hydroxyl groups. However, focusing on this region is very risky because the absorption of atmospheric moisture by a hydroscopic powder after heating is likely to cause ambiguity in the results.

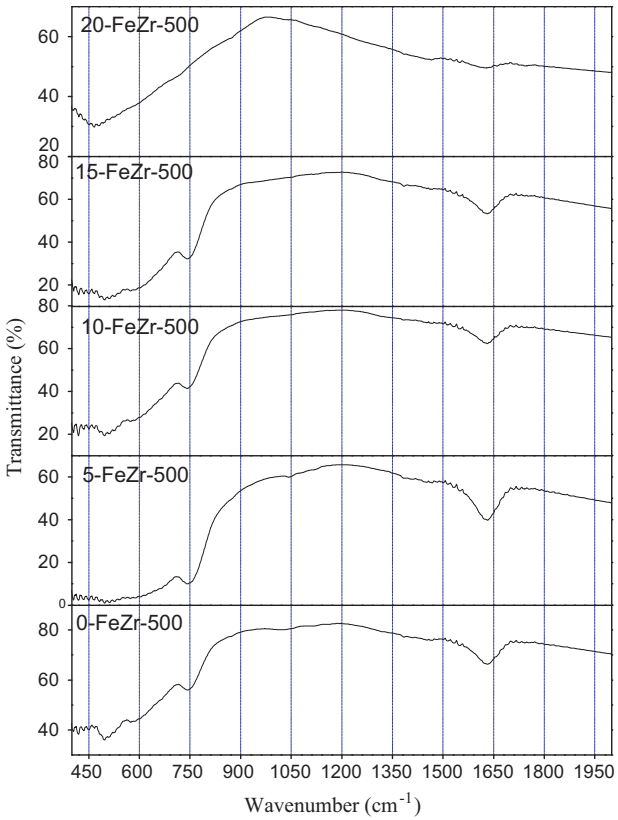

Fig. 9. FTIR spectra of ZrO_2 and iron oxide-supported ZrO_2 catalysts.

Other important FTIR peaks for ZrO_2 and Fe-supported ZrO_2 were found at $740\ cm^{-1}$ and $500\ cm^{-1}$ due to the Zr–O–Zr asymmetric and Zr–O stretching modes, respectively, which are usually the main peaks used to confirm the formation of a ZrO_2 phase [36]. The peak at $750\ cm^{-1}$, corresponding to Zr–O–Zr, completely disappeared in the 20-FeZr-500 sample. It is also interesting to note that the absorption bands due to Fe–O vibration at $475\ cm^{-1}$ and $615\ cm^{-1}$ were not observed in any of the supported samples.

The FTIR spectrum of 20-FeZr-500 showed no IR bands due to Zr or Fe oxides. Okamoto et al. [6] observed that Fe/ZrO_2 shows significantly weaker IR bands than ZrO_2, indicating that the surface –OH groups are extensively consumed on the addition of 5 wt.% Fe. The authors also estimated the –OH group IR band intensities and approximately 65% of the –OH groups were lost for Fe/ZrO_2 sample. In the present study, we also observed the formation of highly dispersed iron oxide species on ZrO_2 in all samples and the contribution of surface Fe species is depended on the Fe oxide loading (XRD and XPS results). In addition to that none of Fe/ZrO_2 samples show any specific IR bands corresponding to iron oxide. Therefore, disappearance of the band at $750\ cm^{-1}$ corresponding to Zr–O–Zr stretching vibration in case of 20FeZr-500 could be due to coverage of ZrO_2 support with Fe surface species. It is noteworthy that Raman spectra of the samples also did not show any peaks corresponding to Fe oxide species.

Garvie [37] reported that in the phase transformation in an infinite single crystal, both the tetragonal and monoclinic phases can coexist as the tetragonal phase grows in the monoclinic matrix. The observations from the HRTEM images of composite particles in the 10-FeZr-500 and 20-FeZr-500 samples provided evidence that a similar process occurred in these catalysts. At a given temperature, the monoclinic-to-tetragonal phase transformation may stop due to the strain energy at the interface boundaries. To continue the phase transformation process, additional thermal energy is required, which can be made available by increasing the pretreatment temperature. In the present study, only the 20-FeZr-500 sample showed complete transformation from the monoclinic to tetragonal phase, even though all of the samples were pretreated at 500 °C. The only parameter that changed during the preparation of the catalysts was the Fe composition. Based on these facts, it is very clear that the amount of Fe plays a crucial role in stabilizing the tetragonal phase. The disappearance of the FTIR peak (Fig. 9) due to the Zr–O–Zr stretching vibration for the 20-FeZr-500 sample indicates that at 20 wt.% loading, Fe cations replace some Zr cations in the crystal lattice and stabilize the tetragonal structure.

It appears that only isolated and disordered Fe^{3+} cations located on the ZrO_2 surface are present when the Fe concentration is $\leq$15 wt. %, as indicated by the presence of a Fe $2p_{3/2}$ peak without any satellite peak. This conclusion is in good agreement with the results reported by Kriventsov et al. [11]. These authors characterized the catalysts using EXAFS and concluded that the iron was located on the external surface of the (1 1 1) plane of the ZrO_2 nanoparticles as isolated ions at concentrations less than one monolayer, and when they used higher Fe loadings, iron produced a two-dimension layer structure.

The oxygen vacancies associated with Zr can provide stability for *t*-ZrO_2. This effect has been explained by the large disturbance in the crystal lattice produced by the incorporation of Fe^{3+}, which competes with Zr ions for the oxygen vacancies [38]. Additionally, it seems that this effect is related to the preparation and pretreatment conditions [39]. In previous studies, researchers observed that the crystallization process in pure ZrO_2 samples resulting in the formation of the monoclinic phase is initiated at approximately 350 °C. This indicates that in addition to influencing the nature of the phase, the presence of iron increases the crystallization temperature in this process, as shown in the TG and DSC measurements. Crystalline iron oxides or mixed oxide phases such as α-Fe_2O_3 or $FeZrO_5$ were not found in the Fe-supported samples, even in the more concentrated ones (20 wt.% loading). This suggests that, in contrast to the Fe/ZrO_2 systems previously studied by Navio et al. [12], a high loading of iron oxide is needed to complete the monolayer coverage of mesoporous ZrO_2. Application of the synthesized materials as potential catalysts for the decomposition of NH_3 and selective catalytic reduction of NO_x is underway in our laboratory.

4. Conclusions

Nanosized mesoporous ZrO_2-supported iron oxide materials were successfully prepared using a modified co-precipitation method. The ZrO_2 calcined at 500 °C was found to exist in two phases, monoclinic and tetragonal. The addition of iron oxide (5–20 wt.%) enhanced the formation of the tetragonal ZrO_2 phase. XRD and Raman spectroscopy results confirmed that the addition of 20 wt.% iron oxide produced complete phase transformation from the monoclinic to tetragonal phase. A significant decrease in the pore size and surface area was observed with the 20 wt.% iron oxide-loaded sample. Observation of a satellite XPS peak corresponding to the Fe^{3+} of Fe_2O_3 and disappearance of the Zr–O–Zr stretching vibration in the FTIR analysis of the 20 wt.% iron oxide-loaded sample indicated the formation of amorphous Fe_2O_3 on the surface of the ZrO_2 support and migration of Fe cations from the surface to the crystal lattice of ZrO_2 to stabilize the tetragonal phase.

Acknowledgments

This project was achieved at King Abdulaziz University – Jeddah and funded by the strategic technologies program for the national science, technology and innovation plan of Saudi Arabia, under grant no. 8-NAN184-3. The authors acknowledge dean of scientific research at King Abdulaziz University for their technical support. The authors are grateful to Felicity Sartain for her discussions and assistance during this research.

References

[1] F. Caruso, Adv. Mater. 13 (2001) 11.
[2] X. Song, A. Sayari, Catal. Rev. Sci. Eng. 38 (1996) 329.
[3] G. Rangarao, Bull. Mater. Sci. 22 (1999) 89.
[4] W. Stichert, F. Schuth, Chem. Mater. 10 (1998) 2020.
[5] J.M. Hermann, J. Disdier, P. Pichat, J. Chem. Soc., Faraday Trans. 77 (1981) 2815.
[6] Y. Okamoto, T. Kubota, Y. Ohto, S. Nasu, J. Phys. Chem. B 104 (2000) 8462.
[7] G. Stefanic, B. Grzeta, S. Musi, Mater. Chem. Phys. 65 (2000) 216.
[8] S. Davison, R. Kershaw, K. Dwight, A. Wold, J. Solid State Chem. 3 (1988) 47.
[9] F.J. Berry, M.H. Loreto, M.R. Smith, J. Solid State Chem. 83 (1989) 91.
[10] I.B. Inwang, F. Chyad, I.J. McColm, J. Mater. Chem. 5 (1995) 1209.
[11] V.V. Kriventsov, D.I. Kochubey, Yu.V. Maximov, I.P. Suzdalev, M.V. Tsodikov, J.A. Navio, M.C. Hidalgo, G. Colon, Nucl. Instrum. Methods Phys. Res. 470 (2001) 341.
[12] J.A. Navio, M.C. Hidalgo, G. Colon, S.G. Botta, M.I. Litter, Langmuir 17 (2001) 202.
[13] W. Ji, Y. Kuo, S. Shen, S. Li, H. Wan, in: Proceedings of the 10th International Congress on Catalysis, Budapest, (1992), p. 2059.
[14] L.A. Boot, A.J. van Dillen, J.W. Geus, F.R. van Bureny, J. Catal. 163 (1996) 186.
[15] Y. Okamoto, T. Kubota, Y. Ohto, S. Nasu, J. Catal. 192 (2000) 412.
[16] J.M.E. Matos, F.M. Anjos Junior, L.S. Cavalcante, V. Santos, S.H. Leal, L.S. Santos Jr., M.R.M.C. Santos, E. Longo, Mater. Chem. Phys. 117 (2009) 455.
[17] R. Srinivasan, B.H. Davis, O.B. Cavin, C.R. Hubbard, J. Am. Ceram. Soc. 75 (2005) 1217.
[18] D.H. Aguilar, L.C. Torres-Gonzalez, L.M. Torres-Martinez, T. Lopez, P. Quitina, J. Solid State Chem. 158 (2001) 349.
[19] V.S. Escribano, E.F. Lopez, M. Panizza, C. Resini, J.M.G. Amores, G. Busca, Solid State Sci. 5 (2003) 1369.
[20] A. Calafat, Stud. Surf. Sci. Catal. 118 (1998) 837.
[21] E.A. El-Sharkawy, A.S. Khder, Micropor. Mesopor. Mater. 102 (2007) 128.
[22] K.V.R. Chary, K.R. Reddy, G. Kishan, J.W. Niemantsverdriet, G. Mestl, J. Catal. 226 (2004) 283.
[23] X. Lu, K. Liang, S. Gu, Y. Zheng, H. Fang, J. Mater. Sci. 32 (1997) 6653.
[24] T. Yamamoto, T. Tanaka, S. Takenaka, S. Yoshida, T. Onari, Y. Takahashi, T. Kosaka, S. Hasegawa, M. Kudo, J. Phys. Chem. B 103 (1999) 2385.
[25] P.D.L. Mercera, J.G. vanOmmen, E.B.M. Doesburg, A.J. Burggraaf, J.R.H. Ross, Appl. Catal. 57 (1990) 127.
[26] D.L.A. de Faria, F.N. Lopes, Vib. Spectrosc. 45 (2007) 117.
[27] D.L.A. de Faria, V. Silva, M.T. de Oliveira, J. Raman Spectrosc. 28 (1997) 873.
[28] S. Shukla, S. Seal, R. Vij, S. Bandyopadhyay, Z. Rahman, Nano Lett. 2 (2002) 989.
[29] C.D. Wagner, D.A. Zatko, R.H. Raymond, Anal. Chem. 52 (1980) 1445.
[30] L.A. Borer, C. Bronnimann, R. Prins, J. Catal. 145 (1994) 516.
[31] C.R. Brundle, Surf. Sci. 66 (1977) 581.
[32] K. Wadelt, Surf. Sci. Rep. 2 (1982) 1.
[33] A.P. Grosvenor, B.A. Kobe, M.C. Biesinger, N.S. McIntyre, Surf. Interface Anal. 36 (2004) 1564.
[34] T. Droubay, S.A. Chambers, Phys. Rev. B 64 (2001) 205414.
[35] B.M. Weckhuysen, D. Wang, M.P. Rosynek, J.H. Lunsford, J. Catal. 175 (1998) 347.
[36] A. Powers, H.B. Gray, Inorg. Chem. 12 (1973) 2721.
[37] R.C. Garvie, J. Phys. Chem. 82 (1978) 218.
[38] S. Fabris, A.T. Paxton, M.W. Finnis, Acta Mater. 50 (2002) 5171.
[39] P. Li, I.-W. Chen, J.E. Penner-Hahn, J. Am. Ceram. Soc. 77 (1994) 1281.